The Astrophysical Journal, 960:3 (12pp), 2024 January 1 https://doi.org/10.3847/1538-4357/ad0842

First X-Ray Polarization Measurement Confirms the Low Black Hole Spin in LMC X-3

Jiří Svoboda[1], Michal Dovčiak[1], James F. Steiner[2], Fabio Muleri[3], Adam Ingram[4], Anastasiya Yilmaz[1,5,6], Nicole Rodriguez Cavero[7], Lorenzo Marra[8], Juri Poutanen[9], Alexandra Veledina[9,10], Mehrnoosh Rahbardar Mojaver[11], Stefano Bianchi[8], Javier A. García[12], Philip Kaaret[13], Henric Krawczynski[14], Giorgio Matt[8], Jakub Podgorný[1,15,16], Martin C. Weisskopf[13], Fabian Kislat[17], Pierre-Olivier Petrucci[18], Maimouna Brigitte[1,5,6], Michal Bursa[1], Sergio Fabiani[3], Kun Hu[7], Sohee Chun[7], Guglielmo Mastroserio[19], Romana Mikušincová[8], Ajay Ratheesh[3], Roger W. Romani[20], Paolo Soffitta[3], Francesco Ursini[8], Silvia Zane[21], Iván Agudo[22], Lucio A. Antonelli[23,24], Matteo Bachetti[25], Luca Baldini[26,27], Wayne H. Baumgartner[13], Ronaldo Bellazzini[26], Stephen D. Bongiorno[13], Raffaella Bonino[28,29], Alessandro Brez[26], Niccolò Bucciantini[30,31,32], Fiamma Capitanio[3], Simone Castellano[26], Elisabetta Cavazzuti[33], Chien-Ting Chen[34], Stefano Ciprini[24,35], Enrico Costa[3], Alessandra De Rosa[3], Ettore Del Monte[3], Laura Di Gesu[33], Niccolò Di Lalla[20], Alessandro Di Marco[3], Immacolata Donnarumma[33], Victor Doroshenko[36], Steven R. Ehlert[13], Teruaki Enoto[37], Yuri Evangelista[3], Riccardo Ferrazzoli[3], Shuichi Gunji[38], Kiyoshi Hayashida[39], Jeremy Heyl[40], Wataru Iwakiri[41], Svetlana G. Jorstad[42,43], Vladimír Karas[1], Takao Kitaguchi[37], Jeffery J. Kolodziejczak[13], Fabio La Monaca[3], Luca Latronico[28], Ioannis Liodakis[44], Simone Maldera[28], Alberto Manfreda[45], Frédéric Marin[15], Andrea Marinucci[33], Alan P. Marscher[42], Herman L. Marshall[46], Francesco Massaro[28,29], Ikuyuki Mitsuishi[47], Tsunefumi Mizuno[48], Michela Negro[49], Chi-Yung Ng[50], Stephen L. O'Dell[13], Nicola Omodei[20], Chiara Oppedisano[28], Alessandro Papitto[23], George G. Pavlov[51], Abel L. Peirson[20], Matteo Perri[23,24], Melissa Pesce-Rollins[26], Maura Pilia[25], Andrea Possenti[25], Simonetta Puccetti[24], Brian D. Ramsey[13], John Rankin[3], Oliver J. Roberts[34], Carmelo Sgrò[26], Patrick Slane[2], Gloria Spandre[26], Douglas A. Swartz[34], Toru Tamagawa[37], Fabrizio Tavecchio[52], Roberto Taverna[53], Yuzuru Tawara[47], Allyn F. Tennant[13], Nicholas E. Thomas[13], Francesco Tombesi[35,54,55], Alessio Trois[25], Sergey S. Tsygankov[9], Roberto Turolla[21,53], Jacco Vink[56], Kinwah Wu[21], and Fei Xie[3,57]

[1] Astronomical Institute of the Czech Academy of Sciences, Boční II 1401/1, 14100 Praha 4, Czech Republic
[2] Center for Astrophysics, Harvard & Smithsonian, 60 Garden Street, Cambridge, MA 02138, USA
[3] INAF Istituto di Astrofisica e Planetologia Spaziali, Via del Fosso del Cavaliere 100, I-00133 Roma, Italy
[4] School of Mathematics, Statistics, and Physics, Newcastle University, Newcastle upon Tyne NE1 7RU, UK
[5] Astronomical Institute of Charles University, Faculty of Mathematics and Physics, Charles University, V Holešovičkách 2, Prague 8, 180 00, Czech Republic
[6] Institute of Theoretical Physics, Faculty of Mathematics and Physics, Charles University, V Holešovickách 2, CZ-180 00 Praha 8, Czech Republic
[7] Physics Department, McDonnell Center for the Space Sciences, and Center for Quantum Leaps, Washington University in St. Louis, St. Louis, MO 63130, USA
[8] Dipartimento di Matematica e Fisica, Università degli Studi Roma Tre, Via della Vasca Navale 84, I-00146 Roma, Italy
[9] Department of Physics and Astronomy, FI-20014 University of Turku, Finland
[10] Nordita, KTH Royal Institute of Technology and Stockholm University, Hannes Alfvéns väg 12, SE-10691 Stockholm, Sweden
[11] Physics Department, Washington University in St. Louis, St. Louis, MO 63130, USA
[12] California Institute of Technology, Pasadena, CA 91125, USA
[13] NASA Marshall Space Flight Center, Huntsville, AL 35812, USA
[14] Physics Department and McDonnell Center for the Space Sciences, Washington University in St. Louis, St. Louis, MO 63130, USA
[15] Université de Strasbourg, CNRS, Observatoire Astronomique de Strasbourg, UMR 7550, F-67000 Strasbourg, France
[16] Astronomical Institute, Charles University, V Holešovičkách 2, CZ-18000, Prague, Czech Republic
[17] Department of Physics and Astronomy and Space Science Center, University of New Hampshire, Durham, NH 03824, USA
[18] Université Grenoble Alpes, CNRS, IPAG, F-38000 Grenoble, France
[19] INAF-Osservatorio Astronomico di Cagliari, via della Scienza 5, I-09047 Selargius (CA), Italy
[20] Department of Physics and Kavli Institute for Particle Astrophysics and Cosmology, Stanford University, Stanford, CA 94305, USA
[21] Mullard Space Science Laboratory, University College London, Holmbury St Mary, Dorking, Surrey RH5 6NT, UK
[22] Instituto de Astrofísicade Andalucía—CSIC, Glorieta de la Astronomía s/n, E-18008 Granada, Spain
[23] INAF Osservatorio Astronomico di Roma, Via Frascati 33, I-00040 Monte Porzio Catone (RM), Italy
[24] Space Science Data Center, Agenzia Spaziale Italiana, Via del Politecnico snc, I-00133 Roma, Italy
[25] INAF Osservatorio Astronomico di Cagliari, Via della Scienza 5, I-09047 Selargius (CA), Italy
[26] Istituto Nazionale di Fisica Nucleare, Sezione di Pisa, Largo B. Pontecorvo 3, I-56127 Pisa, Italy
[27] Dipartimento di Fisica, Università di Pisa, Largo B. Pontecorvo 3, I-56127 Pisa, Italy
[28] Istituto Nazionale di Fisica Nucleare, Sezione di Torino, Via Pietro Giuria 1, I-10125 Torino, Italy
[29] Dipartimento di Fisica, Università degli Studi di Torino, Via Pietro Giuria 1, I-10125 Torino, Italy
[30] INAF Osservatorio Astrofisico di Arcetri, Largo Enrico Fermi 5, I-50125 Firenze, Italy
[31] Dipartimento di Fisica e Astronomia, Università degli Studi di Firenze, Via Sansone 1, I-50019 Sesto Fiorentino (FI), Italy
[32] Istituto Nazionale di Fisica Nucleare, Sezione di Firenze, Via Sansone 1, I-50019 Sesto Fiorentino (FI), Italy
[33] Agenzia Spaziale Italiana, Via del Politecnico snc, I-00133 Roma, Italy
[34] Science and Technology Institute, Universities Space Research Association, Huntsville, AL 35805, USA
[35] Istituto Nazionale di Fisica Nucleare, Sezione di Roma "Tor Vergata," Via della Ricerca Scientifica 1, I-00133 Roma, Italy
[36] Institut für Astronomie und Astrophysik, Universität Tübingen, Sand 1, D-72076 Tübingen, Germany
[37] RIKEN Cluster for Pioneering Research, 2-1 Hirosawa, Wako, Saitama 351-0198, Japan
[38] Yamagata University,1-4-12 Kojirakawa-machi, Yamagata-shi 990-8560, Japan
[39] Osaka University, 1-1 Yamadaoka, Suita, Osaka 565-0871, Japan
[40] University of British Columbia, Vancouver, BC V6T 1Z4, Canada
[41] International Center for Hadron Astrophysics, Chiba University, Chiba 263-8522, Japan
[42] Institute for Astrophysical Research, Boston University, 725 Commonwealth Avenue, Boston, MA 02215, USA
[43] Department of Astrophysics, St. Petersburg State University, Universitetsky pr. 28, Petrodvoretz, 198504 St. Petersburg, Russia

[44] Finnish Centre for Astronomy with ESO, FI-20014 University of Turku, Finland
[45] Istituto Nazionale di Fisica Nucleare, Sezione di Napoli, Strada Comunale Cinthia, I-80126 Napoli, Italy
[46] MIT Kavli Institute for Astrophysics and Space Research, Massachusetts Institute of Technology, 77 Massachusetts Avenue, Cambridge, MA 02139, USA
[47] Graduate School of Science, Division of Particle and Astrophysical Science, Nagoya University, Furo-cho, Chikusa-ku, Nagoya, Aichi 464-8602, Japan
[48] Hiroshima Astrophysical Science Center, Hiroshima University, 1-3-1 Kagamiyama, Higashi-Hiroshima, Hiroshima 739-8526, Japan
[49] Department of Physics and Astronomy, Louisiana State University, Baton Rouge, LA 70803, USA
[50] Department of Physics, University of Hong Kong, Pokfulam, Hong Kong
[51] Department of Astronomy and Astrophysics, Pennsylvania State University, University Park, PA 16801, USA
[52] INAF Osservatorio Astronomico di Brera, via E. Bianchi 46, I-23807 Merate (LC), Italy
[53] Dipartimento di Fisica e Astronomia, Università degli Studi di Padova, Via Marzolo 8, I-35131 Padova, Italy
[54] Dipartimento di Fisica, Università degli Studi di Roma "Tor Vergata," Via della Ricerca Scientifica 1, I-00133 Roma, Italy
[55] Department of Astronomy, University of Maryland, College Park, MD 20742, USA
[56] Anton Pannekoek Institute for Astronomy & GRAPPA, University of Amsterdam, Science Park 904, 1098 XH Amsterdam, The Netherlands
[57] Guangxi Key Laboratory for Relativistic Astrophysics, School of Physical Science and Technology, Guangxi University, Nanning 530004, People's Republic of China

Received 2023 September 19; revised 2023 October 27; accepted 2023 October 28; published 2023 December 18

Abstract

X-ray polarization is a powerful tool to investigate the geometry of accreting material around black holes, allowing independent measurements of the black hole spin and orientation of the innermost parts of the accretion disk. We perform X-ray spectropolarimetric analysis of an X-ray binary system in the Large Magellanic Cloud, LMC X-3, that hosts a stellar-mass black hole, known to be persistently accreting since its discovery. We report the first detection of the X-ray polarization in LMC X-3 with the Imaging X-ray Polarimetry Explorer, and find the average polarization degree (PD) of $3.2\% \pm 0.6\%$ and a constant polarization angle of $-42^\circ \pm 6^\circ$ over the 2–8 keV range. Using accompanying spectroscopic observations by NICER, NuSTAR, and the Neil Gehrels Swift observatories, we confirm previous measurements of the black hole spin via the X-ray continuum method, $a \approx 0.2$. From polarization analysis only, we found consistent results with low black hole spin, with an upper limit of $a < 0.7$ at a 90% confidence level. A slight increase in the PD with energy, similar to other black hole X-ray binaries in the soft state, is suggested from the data but with a low statistical significance.

Unified Astronomy Thesaurus concepts: X-ray binary stars (1811); X-ray observatories (1819); Accretion (14); Astrophysical black holes (98); Black hole physics (159); Spectropolarimetry (1973); High mass x-ray binary stars (733); X-ray astronomy (1810); X-ray detectors (1815)

1. Introduction

Accreting stellar-mass black hole X-ray binaries (BHXRBs) are among the brightest X-ray sources in our Galaxy. While only a few of them are persistent sources, most of them are transients characterized by short, weeks to months, periods of activity and longer, years to decades, quiescent episodes (Frank et al. 2002; Zdziarski & Gierliński 2004). BHXRBs have been found to swing between different spectral states, which are distinguished by broadband spectra and timing characteristics (Zdziarski & Gierliński 2004; Done et al. 2007; Belloni 2010). In the hard state, the spectrum has a power-law-like shape that is believed to be produced by multiple Compton (up-)scattering events of low-energy photons in a hot medium, referred to as a hot accretion flow or a corona. The soft state spectrum resembles blackbody radiation, and is commonly attributed to the multicolor emission of the disk (Novikov & Thorne 1973; Shakura & Sunyaev 1973), which extends down to the innermost stable circular orbit (ISCO). The shape of the spectrum is tightly related to the radius of the ISCO, and by extension, the black hole spin. This property enables the determination of BH spins using the so-called continuum fitting method (Shafee et al. 2006; McClintock et al. 2014).

X-ray polarization offers an alternative means to probe the topology of accreting matter and these measurements have become accessible following the launch of the Imaging X-ray Polarimetry Explorer (IXPE; Weisskopf et al. 2022). The first results on the hard state BHXRB Cyg X-1 suggest the hot medium is extended along the disk plane (Krawczynski et al. 2022), and may have a substantial outflow velocity (Poutanen et al. 2023). Another persistent source Cyg X-3 instead was found to possess an optically thick, elevated envelope resulting from super-Eddington accretion (Veledina et al. 2023).

It has been anticipated that the energy dependence of X-ray polarization degree (PD) and polarization angle (PA) in the soft state sources could be utilized for measuring the black hole spin (e.g., Dovčiak et al. 2008; Schnittman & Krolik 2009; Mikusincova et al. 2023). Polarization in the accretion disk (Rees 1975) can be produced by electron scattering in the upper layers of the disk (a disk atmosphere). In the case of a razor-thin semi-infinite atmosphere, the PD is a known function of the disk inclination (Chandrasekhar 1960; Sobolev 1963). Light bending, relativistic aberration, and frame-dragging effects modify the viewing angles of different parts of the accretion disk, resulting in a characteristic rotation of PA and an overall depolarization, both of which depend on the BH spin (Connors & Stark 1977; Connors et al. 1980).

Yet, the first polarization measurements of a BHXRB in the soft state, 4U 1630-47, revealed severe problems with this standard scenario, as neither a characteristic depolarization nor PA rotation have been observed (Ratheesh et al. 2023). On the contrary, the observed high PD exceeding 8% and its increase with energy pose significant challenges to all existing models. These models thus invariably require parameter adjustments to account for the observed values. Follow-up observation of 4U 1630-47 in the steep power-law state (when both the disk

and Comptonization continuum significantly contribute to the X-ray band) emphasizes the difficulties highlighted by the soft state data (Rodriguez Cavero et al. 2023).

Other IXPE observations of BHXRBs in the soft state include LMC X-1 (Podgorny et al. 2023), 4U 1957+115 (Marra et al. 2023), and Cyg X-1 (Dovciak et al. 2023; J. Steiner et al. 2023, in preparation). LMC X-1 is a low-inclination system ($i \approx 36°$, Orosz et al. 2009). As expected, it has exhibited a low PD of around 1% (Podgorny et al. 2023). In addition, a significant contribution to the polarization was possibly due to a Comptonization component. A higher inclination system, 4U 1957+115 ($i \approx 70°$–$75°$, Hakala et al. 1999), revealed a higher polarization fraction of PD ≈2% (Marra et al. 2023). Overall, the polarization properties of both sources were found to be consistent with theoretical expectations given their inclinations.

The first X-ray polarization measurement of LMC X-3 is the subject of the present study. LMC X-3 is an X-ray binary located in the Large Magellanic Cloud (LMC) at the most recently estimated distance $D = 49.59 \pm 0.09$ (statistical) $\pm$ 0.54 (systematic) kpc (Pietrzyński et al. 2019). The mass of the black hole, companion star, and the inclination of the system are constrained from optical photometric and spectroscopic observations: $M_{\rm BH} = 6.98 \pm 0.56 M_{\odot}$, $M_{\rm star} = 3.63 \pm 0.57 M_{\odot}$, and $i = 69.^{\circ}2$ (Orosz et al. 2014), where $M_{\odot}$ is the mass of the Sun. In the X-rays, LMC X-3 was first detected by the UHURU satellite (Leong et al. 1971) and has subsequently been observed by all major X-ray satellites, owing to its persistent nature. These studies revealed the source to reside primarily in the soft state (Treves et al. 1988; Ebisawa et al. 1993; Nowak et al. 2001), with only rare hard state occurrences (Wilms et al. 2001; Wu et al. 2001) and occasional entry into an anomalous low state characterized by a drop in X-ray flux by a few orders of magnitude (Smale & Boyd 2012; Torpin et al. 2017).

The LMC X-3's soft state spectrum was found to be well modeled by a multicolor disk, whose inner temperature is proportional to the fourth root of the X-ray luminosity (Gierliński & Done 2004). Given the known distance and almost persistent stay in the high/soft state, LMC X-3 has been identified as one of the most promising targets for black hole spin measurements using the X-ray continuum fitting method. Steiner et al. (2010) analyzed a large set of RXTE observations and found a constant inner disk radius until reaching a critical luminosity, found to be around $0.3\,L_{\rm Edd}$ (where $L_{\rm Edd}$ is the Eddington luminosity, $L_{\rm Edd} = 1.26 \times 10^{38} M/M_{\odot}$ erg s^{-1}). For higher luminosities, the measured value for the innermost disk radius increased, indicating a change in the structure of the accretion disk or the disk atmosphere. To account for this behavior, slim disk models were developed (Straub et al. 2011). The slim disk is a solution with the aspect ratio $H/R \lesssim 1$ (where H is the scale height of the disk and R is the radius from the center). However, the apparent increase of the innermost disk radius at high luminosity remained unsolved.

The black hole spin is closely related to the innermost disk radius, assuming the accretion disk extends down to ISCO. The first spin estimates were affected by uncertainty due to the unknown mass of the black hole. More accurate spin measurements were possible only following precise determination of the black hole's mass from optical spectroscopy (Orosz et al. 2014). The spin was measured through the X-ray continuum fitting method as $a \approx 0.2$ (Steiner et al. 2014). The low value of the black hole spin has been subsequently confirmed in more recent analyses (Bhuvana et al. 2022; Yilmaz et al. 2023). Yilmaz et al. (2023) reported a measured value for black hole spin as $a \approx 0.1$. In their analysis, they relaxed the condition of a constant innermost radius at ISCO and showed a scatter of the inner disk radius measurements in different observations during the outbursts (see their Figures 7 and 9).

In this paper, we present the analysis of the first IXPE observations of LMC X-3, showing that the polarimetric data are in line with the low spin of the black hole, previously measured only by X-ray spectroscopy. The observations are described in Section 2. The results of the spectropolarimetric modeling are presented in Section 3 and discussed in Section 4. Section 5 summarizes the main results of the analysis.

2. Observations

LMC X-3 was observed in 2023 July by multiple X-ray instruments. All studied observations are summarized in Table 1. Data reduction and processing are described in more detail in the following sections.

2.1. IXPE

LMC X-3 was observed by IXPE on 2023 July 7–8 and 12–21 (ObsID: 02006599) with a total exposure time 562 ks. IXPE detectors (Soffitta et al. 2021) can measure the Stokes parameters I, Q, and U and they have imaging capabilities, so the source and background regions can be spatially separated. Level 2 event files were downloaded from the HEASARC and then filtered for source and background regions using the `xpselect` tool from the IXPEOBSSIM software package version 30.5 (Baldini et al. 2022). The source extraction regions were selected for each detector unit as circles with a radius of 60″. The background regions were defined as annuli with an inner radius of 180″ and an outer radius of 280″.

Polarization cubes were generated using the unweighted `pcube` algorithm (Baldini et al. 2022). We produced PD and PA in five energy bins and obtained significant detection in all bins but the last. We further used the IXPEOBSSIM `PHA1` algorithm to generate the weighted Stokes I, Q, and U parameters with different binning in energy. For the analysis, we used 11 bins (10 bins with a bin size 0.5 keV in the 2–7 keV energy range, and 1 keV bin in 7–8 keV), while for plotting, we used five bins to compare with the unweighted `pcube` results. We used the IXPEOBSSIM unweighted algorithm to further generate Q/I and U/I spectra that were converted to XSPEC-employable FITS spectra with the FTOOL `flx2xsp` with unit response matrices.

2.2. NICER

The Neutron-Star Interior Composition Explorer (NICER) is a soft X-ray timing mission deployed on the International Space Station (ISS). NICER is composed of 52 silicon-drift detectors, sensitive from ∼0.2 to 12 keV, with <100 ns timing fidelity (Gendreau et al. 2012). Each detector is paired with a single-bounce reflector optic, all mutually co-aligned on the sky. NICER carried out two observations of LMC X-3 during the IXPE campaign, on 2023 July 8 and 17, corresponding to OBSIDs 6101010117 and 6101010118, respectively. These observations were obtained after one of the detector thermal shields was damaged in 2023 May, which resulted in a light leak during ISS daytime, which resulted in optical loading of

Table 1
List of Observations

Observatory	Instrument	Observation ID	Start Date	End Date	Net Exposure (ks)
IXPE	GPD	02006599	2023-07-07 18:42:31	2023-07-09 13:39:07	105.2
		02006599	2023-07-12 16:55:48	2023-07-20 14:19:34	458.6
NICER	XTI	6101010117	2023-07-08 10:10:50	2023-07-08 16:34:40	2.14
		6101010118	2023-07-17 23:37:19	2023-07-17 23:40:14	0.16
NuSTAR	FPMA/FPMB	309020041002	2023-07-09 12:16:09	2023-07-09 23:51:09	27.6
		309020041004	2023-07-14 07:56:09	2023-07-15 06:31:32	28.1
		309020041006	2023-07-19 19:41:09	2023-07-21 07:16:23	29.0
Swift	XRT	00089714001	2023-07-09 19:29:38	2023-07-09 19:31:50	1.3
		00089714002	2023-07-14 02:50:08	2023-07-14 16:54:56	1.8
		00089714003	2023-07-20 01:21:15	2023-07-20 04:42:56	1.9

the detectors, producing an increase in noise and potential packet losses.[58]

LMC X-3 could only be observed during ISS daytime, and as a result, we found it necessary to use nonstandard filtering to recover usable data. For both observations, 42 of NICER's 52 detectors were turned on. We screened the active detectors for outlier behavior on the basis of rates of X-ray, overshoot, and undershoot events, flagging >10-(robust) σ outliers from the detector ensemble. This resulted in discarding all data from between one and seven detectors per continuous GTI interval. We obtained a useful exposure time of ≈2.2 ks and ≈160 s, for the two observations, respectively, and were initially extracted separately per continuous GTI segment. After checking their mutual consistency, we merged them together for the spectral analysis. In order to avoid contamination from low-energy noise events, which are exacerbated by the light leak, we restrict our analysis to an energy range >0.5 keV. Response products were generated based on the number of active detectors, and rates were adjusted for $\gtrsim$1% detector dead time caused primarily by optical-loading events.

Because NICER is non-imaging, the spectral background is determined via various empirical models (Remillard et al. 2022). We adopt the `SCORPEON` background model,[59] and is normalized to the number of selected detectors.

2.3. NuSTAR

Three accompanying observations by the NuSTAR satellite (Harrison et al. 2013) were performed at the beginning, in the middle, and at the end of the IXPE observation with a total net exposure time of ≈85 ks, see more details in Table 1. NuSTAR data were reduced using the standard Data Analysis Software (`NuSTARDAS`). The NuSTAR calibration files available in the CALDB database were used to calibrate the cleaned event files, produced by the `nupipeline` task. The source regions were selected as circles with a radius of 60″ centered on the source image, and background regions with a radius of 90″ were selected from the corner of the same quadrant in the source-free region. The source spectrum is soft and background dominates over the source above 20 keV. Therefore, we limit the NuSTAR data of LMC X-3 at high energy to be below 20 keV in all spectral analyses.

[58] https://heasarc.gsfc.nasa.gov/docs/nicer/analysis_threads/light-leak-overview/
[59] https://heasarc.gsfc.nasa.gov/docs/nicer/analysis_threads/scorpeon-overview/

2.4. Neil Gehrels Swift Observatory

Simultaneous to NuSTAR, the Neil Gehrels Swift Observatory (Gehrels et al. 2004) observed LMC X-3 with exposure times of 1.3 ks (ObsID: 00089714001, 2023 July 9), 1.8 ks (ObsID: 00089714002, 2023 July 14), and 1.9 ks (ObsID: 00089714003, 2023 July 20). Individual X-ray Telescope (XRT; Burrows et al. 2005) spectra were extracted using the standard online tools provided by the UK Swift Science Data Centre (Evans et al. 2009) using a source region of 60″ radius centered at the source location.

2.5. Software Tools for Data Analysis

We used the HEASOFT[60] software package (Blackburn 1995), version 6.31, for the data reduction and rebinning, and the XSPEC software package (Arnaud 1996), version 12.13, for the spectral analysis. We rebinned all the NICER, NuSTAR, and Swift data with the tool `ftgrouppha` and applied optimal binning (Kaastra & Bleeker 2016) together with the condition for a minimum signal-to-noise ratio to be equal to 3. For the time-averaged spectral fits, we combined observations from multiple exposures using ADDSPEC.PY.[61] Across the entire paper, the errors are quoted as 90% confidence levels if not stated otherwise.

3. Results

3.1. X-Ray Polarimetric Measurements

The IXPE light curve is shown in Figure 1. LMC X-3 shows a steady continuous increase of the flux during the exposure. The count rate (averaged over all three GPDs) increased from about 1.2 cts s^{-1} at the beginning of the observation to 1.5 cts s^{-1} at the end of the observation. The polarization is characterized by the Stokes Q and U parameters divided by the Stokes parameter I (total number of counts). The Q/I and U/I light curves are shown in the middle panels of Figure 1. The variations observed are consistent with statistical fluctuations only, with a successful joint fit of a constant to both Q/I and U/I light curves achieving $\chi^2/\mathrm{dof} = 153.7/166$. There is also no evidence for any significant changes in the spectral hardness, defined as the difference between counts in the hard (4–8 keV) and soft (2–4 keV) energy bands divided by the total number of counts in the 2–8 keV band, as shown in the bottom panel of Figure 1.

[60] https://heasarc.gsfc.nasa.gov/docs/software/lheasoft/
[61] https://github.com/JohannesBuchner/BXA

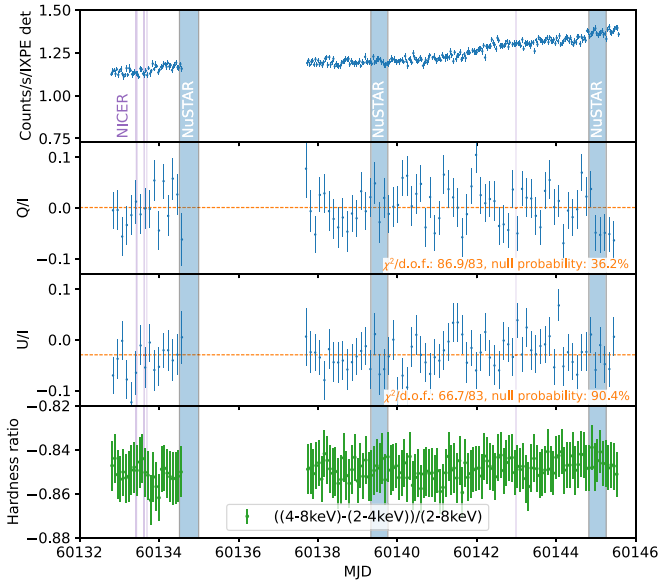

Figure 1. IXPE light curve: variation of the counts (top panel), normalized Stokes parameters Q/I (second panel) and U/I (third panel), and spectral hardness (bottom panel), as a function of time (in Modified Julian Date). The dates of the accompanying observations by NICER and NuSTAR are indicated as shaded regions.

Using the time-integrated measurements of the Stokes parameters, we derived the PD and PA using the `xpbin` tool within the `pcube` algorithm. The average 2–8 keV PD for all three detectors is PD $=3.1\% \pm 0.4\%$, and the PA $= -45° \pm 4°$ with the 1σ errors. The measurements are above the so-called minimum detectable polarization, MDP_{99}, which is the degree of polarization, for which the probability of the detection of the corresponding amplitude modulation only by chance is 1% (Weisskopf et al. 2010). In our observation $\mathrm{MDP}_{99} = 1.23\%$ in 2–8 keV. The energy dependence of PD and PA is shown in Figure 2, with the data binned in five energy bins. Measurement of the polarization above the MDP_{99} is achieved in the entire band with the exception of the highest energy bin (6.5–8 keV), where the MDP_{99} is higher than the actual measurement. In the 2–5 keV energy band, the PD is around 3%. An increasing trend of polarization with energy is apparent from the plot, but the measurement uncertainty gets significantly larger (see more in Section 4). The PA is consistent with being a constant with only possible small deviations at higher-energy bins.

3.2. X-Ray Spectral Analysis

To properly model and interpret the polarization measurements, a robust spectral fit is first needed. For this purpose, the long IXPE observation was accompanied by several exposures with sensitive instruments suitable for a broadband spectroscopic analysis (see Table 1).

3.2.1. A Quick-look Analysis of the NICER, NuSTAR, and Swift Accompanying Spectra

We first analyzed the NICER, NuSTAR, and Swift spectra using a simple absorbed multicolored disk blackbody emission (Mitsuda et al. 1984) and power-law component for the Comptonization, which allows us to estimate the disk temperature and the fraction of the Comptonized emission in the X-ray spectra. We used the `tbabs` model to account for absorption in the line of sight in our Galaxy (Wilms et al. 2000) and fixed the value of the hydrogen column density to $N_{\mathrm{H}} = 4.5 \times 10^{20}$ cm^{-2} from a full sky H I survey (HI4PI Collaboration et al. 2016). We further add a cross-normalization factor to account for changes between different instruments. The model in XSPEC notation is `const*tbabs*(diskbb + powerlaw)`. The disk temperature as well as the power-law photon index values were linked between different instruments and also between different exposures. Only the normalization factors of both components (disk blackbody and power law) were allowed to vary to determine if there is any spectral variability and of which component.

We found that the spectrum is dominated by the disk blackbody emission with the Comptonization component significant only for NuSTAR observations that have a coverage above 10 keV, see Figure 3. For the inner disk temperature, we obtained the value $kT \approx 1.1$ keV. We get the power-law photon index of $\Gamma \approx 2.4$. The NuSTAR observations reveal a clear variability of the Comptonization component above ≈15 keV. The simple `diskbb + powerlaw` model allows us to estimate the fraction of the Comptonized emission, which is less than 1% in 2–8 keV. The model decomposed in the two components is plotted in Figure 3 for the three NuSTAR observations. The strongest Comptonization component is measured in the last observation. However, it is evident from the plot that the Comptonization contributes very little to the IXPE 2–8 keV energy band, and thus we can assume that the measured polarization is related to the main component, which is the thermal emission of the accretion disk.

From comparing the three Swift spectra, we see that there is no significant variability in the soft X-ray band, confirming the results suggested by the IXPE hardness ratio shown in Figure 1. The only apparent but small difference is around 1.5 keV between the first and the other two observations (see the bottom panel of Figure 3). Any further investigation of this discrepancy is beyond the scope of this analysis, and therefore, we limited the Swift spectra to be in the 2–8 keV energy range for further spectral analysis with the merged spectra (Section 3.2.2). Similar discrepancies below 2 keV are likewise seen between Swift and NICER measurements. These residuals lead to a fit that is not formally acceptable, with a chi-square value of $\chi^2 = 1255$ for 411 degrees of freedom ($\chi^2_{\mathrm{red}} \approx 3$).

3.2.2. Spectral Analysis with Relativistic Models for the Accretion Disk Emission

Owing to the detection of little spectral variability, we further use merged Swift and NuSTAR spectra. There are known calibration uncertainties with the IXPE spectra, and we therefore applied the `gain` model to fit the offset slope and intercept for IXPE. We further performed a spectral analysis of seven data sets (one NICER, two NuSTAR detectors FPMA and FPMB, one Swift, and three detectors of IXPE) with a cross-calibration constant fixed to 1 for NICER and allowed to vary between 0.8 and 1.2 for the other detectors. Figure 4 shows the time-averaged spectra of different detectors in the first (top) panel.

We first employed a relativistic accretion disk model `kerrbb` (Li et al. 2005) convolved with a nonrelativistic Comptonization model `simpl` (Sunyaev & Titarchuk 1980; Steiner et al. 2009), allowing for both up- and down-scattering. For absorption, we employed the `tbfeo` model allowing for

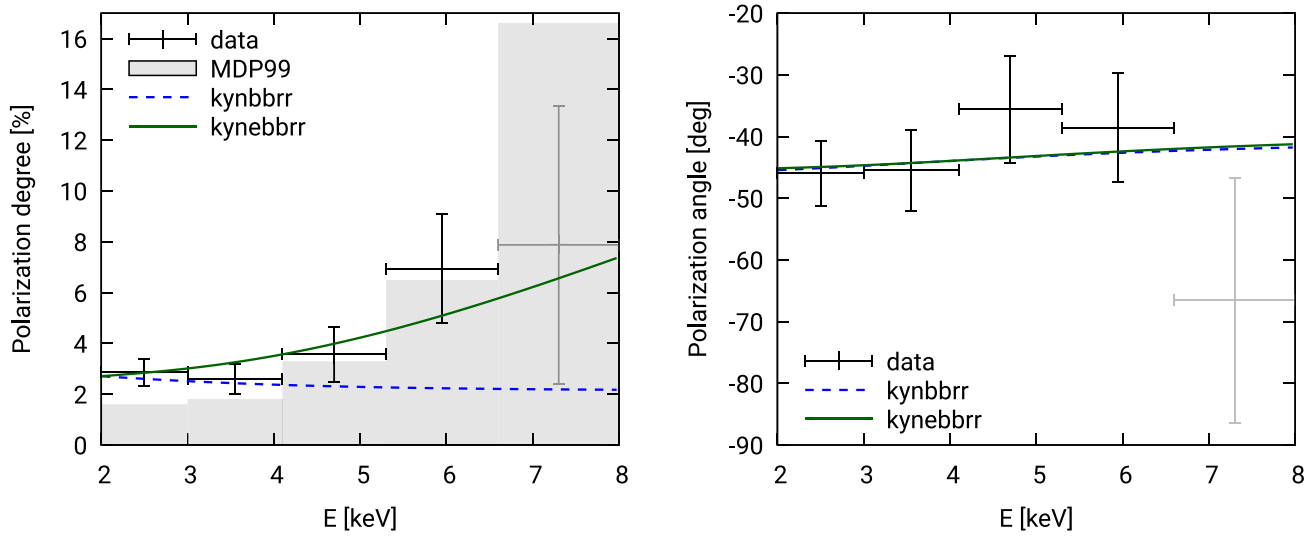

Figure 2. Measured PD (left) and PA (right) shown with 1σ error bars. The shaded area in the PD-plot shows an estimate of the MDP_{99}, showing the significant polarization measurements from 2 keV up to ≈6.5 keV. The dashed (blue) and dotted–dashed (green) lines show the best-fit models to polarimetric Q/I and U/I data with the relativistic thermal disk emission models (see Sections 3.4 and 4).

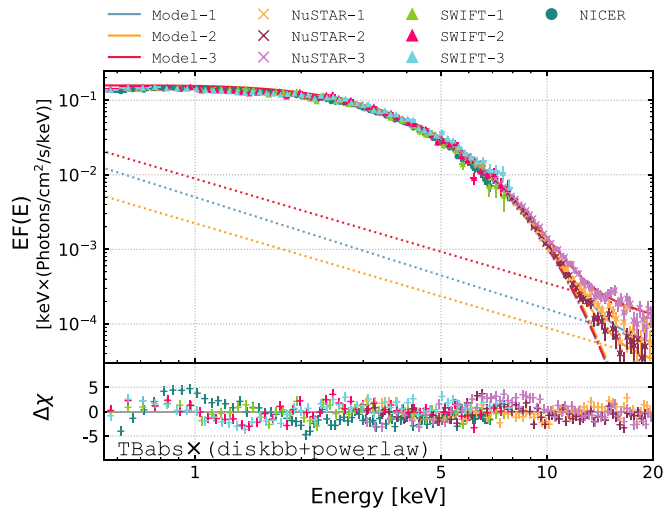

Figure 3. Top: unfolded spectra (`plot eufspec` in XSPEC) with a joint spectral fit using the simple absorbed `diskbb+powerlaw` model employing the NICER and three Swift and NuSTAR exposures. Bottom: the residuals of the data from the model.

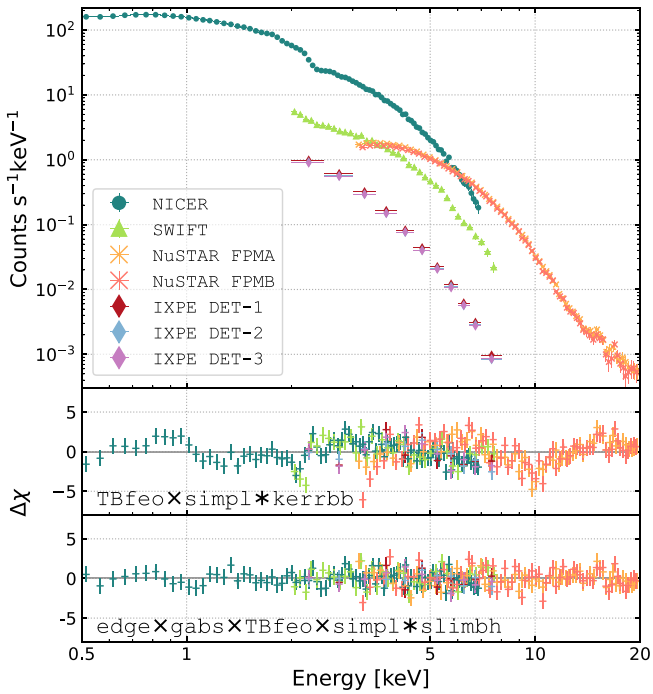

Figure 4. Top: time-averaged NICER, NuSTAR, Swift, and IXPE data. Middle: the residuals of the data from the model using `tbfeo×simpl * kerrbb`. Bottom: the residuals of the data from the final best-fit model.

different oxygen and iron abundances. Because the LMC is a low-metallicity environment, we let the abundances be in the interval 0.25–1. The fit converged to $N_{\rm H} \approx 0.03 \times 10^{22}$ cm^{-2} with the oxygen and iron abundances being pegged at their low-value limits at 0.25. We note that since the column density is lower than the column density expected in the line of sight in our Galaxy, the low oxygen and iron abundances may be an artifact of calibration uncertainties in the 0.5–1 keV band for NICER and/or due to variations of the absorption column within our Galaxy. No evidence for local absorption is consistent with LMC X-3's location at a large distance from the center of the LMC, away from any gaseous nebulae.

With the `tbfeo*simpl*kerrbb` model, we obtained the dimensionless black hole spin $a = 0.20 \pm 0.02$, accretion rate $\dot{M} \approx (4.5\text{–}5.6) \times 10^{18}$ g s^{-1}, and the photon index pegged at $\Gamma = 2.0$, which was the lowest allowed value. We allowed the hardening factor of the `kerrbb` model to vary and we obtained $h_d \approx 1.7$ for NuSTAR and $h_d \approx 1.9$ for NICER. The fit was formally not acceptable with $\chi^2/\nu = 676/274 \approx 2.5$, mainly due to discrepancies between NICER and NuSTAR data, whose residuals had opposite slopes in the overlapping energy band (see the second panel of Figure 4 at 3–8 keV energy band).

The lowest measured accretion rate 4.5×10^{18} g s^{-1} corresponds to the luminosity $L = \eta \dot{M} c^2 \approx 0.3\, L_{\rm Edd}$, where η is the accretion efficiency $\eta \approx 0.065$ (for $a = 0.2$). At such a luminosity, LMC X-3 might deviate from the standard thin disk model, and a slim disk scenario was proposed to take place at the high-luminosity regime (Straub et al. 2011). Therefore, we replaced the `kerrbb` model with the `slimbh` model (Sądowski et al. 2011; Straub et al. 2011), and we obtained a

Table 2
Spectral Fit Parameters with the Final Preferred Spectral Model

Component	Parameter (units)	Description	Value			
			NICER	NuSTAR	Swift	IXPE
TBfeo	$N_{\rm H}$ (10^{22} cm^{-2})	H column density		0.046 ± 0.003		
	O	Abundance		0.3 ± 0.2		
	Fe	Abundance		0.8 ± 0.4		
SLIMBH	$M_{\rm bh}$ ($M_\odot$)	Black hole mass		6.98 (frozen)		
	a/M	Black hole spin		0.19 ± 0.02		
	$L_{\rm Edd}$	Luminosity	0.40 ± 0.01	0.43 ± 0.01	0.41 ± 0.02	$0.50^{+0.02}_{-0.04}$
	i (deg)	Inclination		69.2 (frozen)		
	α	Viscosity		0.1 (frozen)		
	$D_{\rm bh}$ (kpc)	Distance		49.59 (frozen)		
	hd	Color hardening		-1 (i.e., using TLUSTY)		
	$l_{\rm flag}$	Limb darkening		0 (frozen)		
	$v_{\rm flag}$	Self-irradiation		0 (frozen)		
	norm	Normalization		1 (frozen)		
SIMPL	Γ	Photon index		2.7 ± 0.3		
	FracSctr	Scattered fraction		$0.012^{+0.001}_{-0.002}$		
χ^2/dof				$277/265 \approx 1.04$		

Note. The final model in the XSPEC notation is `constant*edge*gabs*tbfeo*simpl*slimbh`. Model parameters for cross-calibration and instrumental features are summarized in Table 3.

significantly better fit with $\chi^2/\nu = 414/277 \approx 1.5$. The `slimbh` model improved the consistency of the data residuals between NICER and NuSTAR.

The only residuals were now narrow features around 2 and 2.4 keV for NICER and 10 keV for NuSTAR, which can be seen in the second panel of Figure 4. Similar residuals in the NICER data were reported in some previous analyses and attributed to calibration uncertainties, see, e.g., Wang et al. (2021) and NICER calibration documentation.[62] The 10 keV dip in the NuSTAR data is not apparent in a simple `diskbb +powerlaw` fit (see Figure 3), and is thus most likely a model-dependent feature present in residuals of both the `simpl* kerrbb` and `simpl*slimbh` models. A similar feature was also reported in the analysis of LMC X-1 with the `kerrbb + nthcomp` model (Podgorny et al. 2023), suggesting its relation to an interplay between a high-energy tail of the relativistic thermal disk emission model and Comptonization. For our final model, we account for the 2 and 10 keV features with narrow Gaussian absorption lines and the 2.4 keV feature with a *smeared-edge* component. The goodness of the final fit is $\chi^2/\nu = 277/265 \approx 1.04$. The residuals from the best-fit model are shown in the third panel of Figure 4.

The values of the best-fit model are summarized in Table 2. The spin value is consistent with the measurements using the `kerrbb` model, $a \approx 0.20 \pm 0.02$. The spectral hardening in the `slimbh` model is not a free parameter, but is instead calculated using the vertical structure computed using the TLUSTY code (Hubeny & Lanz 1995). The estimated luminosity is in the range of $L = 0.40$–$0.45\,L_{\rm Edd}$ depending on which detector is considered (the slightly higher value for IXPE can be, however, affected by the fitted cross-calibration constants lower than 1). The parameters of the Comptonization model `simpl` were constrained well only from the NuSTAR spectra, and therefore, we linked the values between the different detectors. The photon index is $\Gamma = 2.7 \pm 0.3$ and the scattering fraction is $0.012^{+0.001}_{-0.002}$. Similarly, absorption was best constrained from the NICER data and we linked the absorption parameters for the different detectors to it.

In our preferred model, the black hole mass and inclination are initially fixed to the values from the dynamical measurements (Orosz et al. 2014). Because in the IXPE observation of Cyg X-1 the inclination of the innermost accretion disk from the X-ray spectroscopy and polarimetry was found to be different from the value for the orbital inclination (Krawczynski et al. 2022), we also performed an alternative spectral fit with free inclination. The best-fit value of the inclination changed slightly to $i = 71.8^{+2.0}_{-1.2}$ deg, and the corresponding inferred luminosity increased from $L = 0.43\,L_{\rm Edd}$ to $L = 0.48\,L_{\rm Edd}$. The goodness of the fit improved by $\Delta\chi^2 = 310$–$317 = -7$ compared to the initial fit. This improvement was only marginal and we conclude that the inclination of the accretion disk constrained from the X-ray spectra is consistent with the inclination of the binary system constrained from the optical measurements.

3.3. Spectropolarimetric Analysis

We first included the IXPE Q and U spectra in our analysis by taking our best-fitting spectral model from Table 2 and assigning a constant PD and PA to it using the `polconst` model. For Q and U spectra, we applied the same gain as for I spectra, and we also kept the cross-normalization factors. The only free parameters were the PD and PA, noted as A and ψ in the `polconst` model. Considering the full IXPE bandpass yields a PD of $A = 3.2\% \pm 0.6\%$ and a PA of $\psi = -42° \pm 6°$.

To test whether the polarization is increasing linearly with the energy, we replaced the `polconst` model by `pollin` and fitted the 2–8 keV I, Q, and U spectra. The polarization fraction in the `pollin` model is parametrized with the polarization fraction at 1 keV, A_1, and the slope $A_{\rm slope}$. We obtained a

[62] https://heasarc.gsfc.nasa.gov/docs/heasarc/caldb/nicer/docs/xti/NICER-xti20221001-Release-Notes.pdf

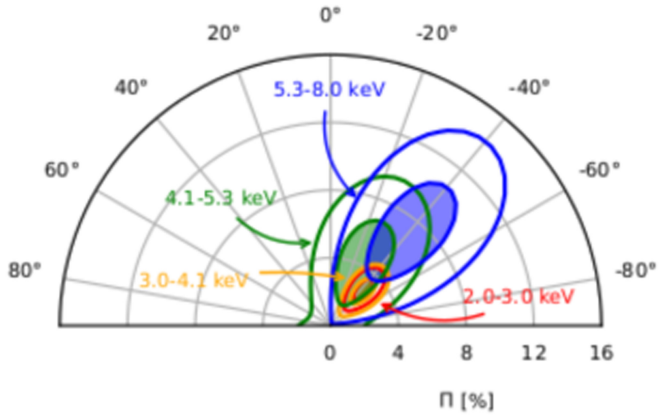

Figure 5. Polar plot of the polarization measured in different energy ranges with the spectral best-fit model. The filled contours correspond to the 68% (1σ) and the outer contours to the 99.9% confidence levels, respectively.

similarly good fit as with the `polconst` model with $A_{\rm l} = 1^{+2}_{-1}\%$ and $A_{\rm slope} = (6 \pm 6) \times 10^{-3}$, i.e., being consistent with the polarization being constant. The statistical improvement is only marginal with $\Delta\chi^2 \approx 2$ for one additional free parameter, giving the F-test probability ≈0.4 that the improvement is just coincidental.

To investigate any (other than linear) energy dependence, we performed the fit in four different energy bands spanning 2–8 keV and calculated contours using 50 steps in each parameter. We defined the energy bands as 2–3, 3–4.1, 4.1–5.3, and 5.3–8 keV. Figure 5 shows the resulting contours in the polar plot of PD and PA. While there is an apparent trend of increasing PD with the energy as in Figure 2, the significance of the change is not high. The PD is consistent with being a constant below 5 keV, and increases with energy above 5 keV only at the 1σ confidence level.

We then proceeded to fit physical models that self-consistently predict energy-dependent polarization properties. Since no polarized slim disk model currently exists, we were limited to fitting standard thin disk models. We employed models from the relativistic package KY (Dovčiak et al. 2004), which has been developed for spectral, timing, and polarimetry analysis. For simplicity, we neglected the contribution due to the Comptonization that is less than 1% in the 2–8 keV energy range (see Figure 3). We employed the relativistic thin Novikov–Thorne disk model `kynbbrr` (Taverna et al. 2020; Mikusincova et al. 2023). This includes the same parameters as `kerrbb`, with some extra parameters required to specify the polarization properties such as the position angle of the disk (and black hole) rotation axis on the plane of the sky χ_0, the optical depth of electron scattering in the disk atmosphere τ, and the albedo that defines the reflectivity of the disk surface for returning radiation (radiation that is lensed by a black hole such that it returns and reflects on the other part of the disk before reaching an observer). The `Stokes` parameter in the model allows us to define how the polarization is calculated. We used `Stokes` $= -1$, which reads the polarization from loaded I, Q, and U spectra.

A joint fit of the IXPE I, Q, and U spectra provided an acceptable fit with $\chi^2/\nu = 102/95$ using the `const*tbfeo*kynbbrr` model. The parameters of the absorption, cross-normalization constants, and gain parameters were fixed to the values from the previous global spectral fit (see Tables 2 and 3). The only free values in the `kynbbrr` model were black hole spin, measured as $a = 0.1 \pm 0.1$, the accretion rate $\dot{M} = 0.45^{+0.07}_{-0.04}\, M_{\rm Edd}$, the position angle of the disk rotation axis $\chi_0 = 47^\circ \pm 6^\circ$, and the normalization parameter $N_{\rm K} = 0.042 \pm 0.005$. The accretion rate $\dot{M} \approx 0.45\, M_{\rm Edd}$ is consistent with the previous finding using the `kerrbb` and `slimbh` models. The normalization in the `kynbbrr` model would be 1 for a source at a distance of 10 kpc. The distance of LMC X-3 is ≈50 kpc, and thus, the normalization value is expected to be around $1/5^2 \approx 0.04$, consistent with the measurement.

3.4. Black Hole Spin Measurements from the Polarimetry

For fitting the black hole spin from the polarimetric measurements only, independently of the total spectrum, we employed the normalized Q/I and U/I spectra, to which we applied the `kynbbrr` model with the normalization fixed to 1. The `Stokes` parameter in the `kynbbrr` model, which is a switch parameter defining the output of the model, needs to be set to 8 for Q/I and 9 for U/I, respectively. The normalization in this case needs to be set to 1. We fixed the accretion rate to $\dot{M} = 0.45 M_{\rm Edd}$. We tested two cases of albedo, 0 and 1. While the albedo = 0 means that no returning radiation is taken into account, albedo = 1 corresponds to the 100% reflectivity of the gravitationally light-bended returning radiation. The albedo is important mainly for a highly spinning black hole when the ISCO extends closer to the black hole and more returning radiation is expected (Cunningham 1976).

For the albedo equal to 0, we fitted the Q/I and U/I spectra with the black hole spin a and χ_0 as free parameters. We obtained a perfectly acceptable fit with $\chi^2/\nu = 19.9/20 \approx 1.0$, $a < 0.66$, and $\chi_0 = 44.^\circ6 \pm 6.^\circ4$. The energy-dependent PD and PA output of this model is plotted in Figure 2 by a dashed (blue) line. For a nonzero value of the albedo, the model is currently calculated for 20 values of the spin and does not allow for a direct fitting of this parameter. We applied the `steppar` command in XSPEC to calculate the χ^2 values for the different values of the black hole spin, and for the comparison, we performed the same procedure for albedo equal to 0.

Figure 6 shows the dependence of the fit goodness against the spin value for the two cases with albedo equal to 0 and 1, respectively. With 90% confidence, the black hole spin is required to be lower than 0.66 for albedo = 0 and lower than 0.3 for albedo = 1. The case of albedo = 0 is preferred by the fit with lower χ^2 values. The results indicate that the sole polarimetry measurements are consistent with the low black hole spin in LMC X-3, independently of the spectral fitting.

4. Discussion

With the best-fit spectral model, we obtained for the polarimetry PD = 3.2% ± 0.6% and PA = −42° ± 6° in the 2–8 keV energy band, assuming a constant polarization over energy. These measurements are in perfect agreement with the values (PD = 3.1% ± 0.4% and PA = −45° ± 4°) obtained from an alternative analysis using the `xpbin` tool within the `pcube` algorithm (see Section 3.1).

Regarding the PA measurements, there are no known large-scale physical structures associated with LMC X-3 with which to compare the PA. LMC X-3 is persistently in the high/soft state and no jet has been detected in the radio despite several efforts (Fender et al. 1998; Gallo et al. 2003; Lang et al. 2007). There is also no evidence for ionization cones in the far-UV

Table 3
Modeling Cross-calibration and Instrumental Features in the Final Spectral Fit

Component	Parameter	NICER	NuSTAR		Swift	IXPE		
			FPMA	FPMB		GPD 1	GPD 2	GPD 3
CONSTANT		1 (frozen)	1.18 ± 0.03	1.16 ± 0.03	1.23 ± 0.07	0.88 ± 0.02	0.86 ± 0.02	0.81 ± 0.02
GABS	E (keV)	2.07 ± 0.04	9.9 ± 0.1		2.14 ± 0.04		⋯	
	σ (keV)	$0.08^{+0.02,\text{pegged}}_{-0.06}$	0.1 (pegged)		0.03 ± 0.03		⋯	
EDGE	E (keV)	2.35 ± 0.05	⋯		⋯		⋯	
	τ (keV)	0.02 ± 0.02	⋯		⋯		⋯	
GAIN	slope	⋯	⋯		⋯	$0.95^{+0.02}_{-0.01}$	0.96 ± 0.01	$0.95^{+0.02}_{-0.01}$
	offset (keV)	⋯	⋯		⋯	$0.08^{+0.02}_{-0.04}$	$0.05^{+0.03}_{-0.04}$	$0.07^{+0.03}_{-0.04}$

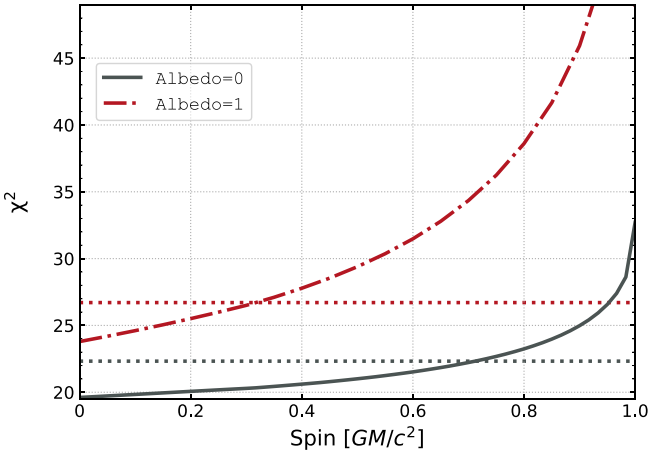

Figure 6. Polarimetry constraints of the black hole spin, expressed as the goodness of the fit (as the χ^2 values) vs. black hole spin from Q/I and U/I fitting with the `kynbbrr` model for two extreme values of albedo: 0 (black solid line) and 1 (red dotted–dashed line). The dotted horizontal lines represent 90% confidence levels.

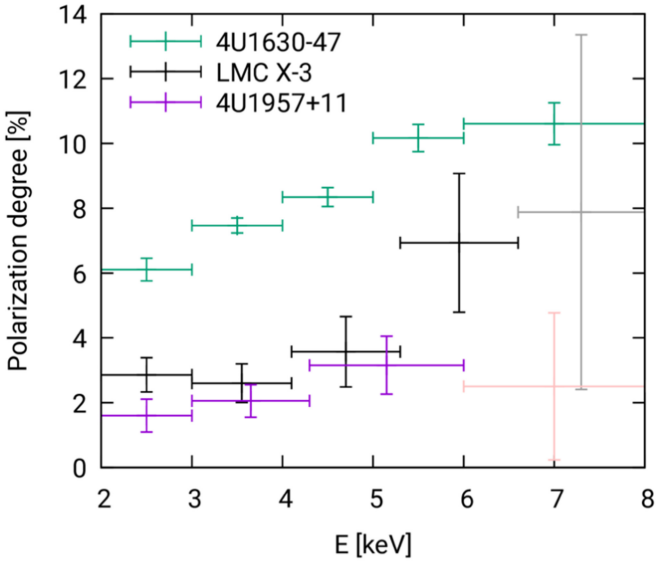

Figure 7. Comparison of the energy dependence of the PD in X-ray binaries in the high/soft state dominated by the thermal emission of the accretion disk.

(Hutchings et al. 2003), or the presence of any significant emission or absorption lines in soft X-rays (Page et al. 2003).

The level of the PD is consistent with expectations for the thermal disk emission around a black hole with a low spin and high inclination (see the case of $a = 0$ and $i = 70°$ in Figure 4 in Mikusincova et al. (2023) with a constant PD just slightly below 3%). The Novikov–Thorne model, assumed in the `kynbbrr` spectral model, provides a reasonably good fit to the X-ray polarimetry despite the best-fit spectral model employing a slim disk. This is most likely explained by the limited statistics of the X-ray polarimetry fit, while the spectral fit is sensitive to small differences between the `kerrbb` and `slimbh` models, which can possibly be attributed to the treatment of the spectral hardening in these models.

The black hole spin, solely constrained from the X-ray polarimetry using normalized Stokes parameters Q/I and U/I, is consistent with the results of determining the spin from the spectral fitting. The constraints on the spin are tighter if the reflection of the returning radiation is taken into account, but even for a model with no reflected returning radiation (albedo = 0), the spin is constrained to be less than 0.7 (see Figure 6).

While the X-ray polarization is well described by the model with constant PD with energy, the data tentatively indicate an increase in the PD with energy, which is most prominently visible in the plot showing the results from the `pcube` analysis (see Figure 2, especially above 5 keV). At higher energies, however, the uncertainty of the polarization measurements increases due to a lower number of counts, and thus in our case, the PD increase with energy is suggested with only marginal statistical significance (see Figure 5).

The increasing energy dependence is included in the model variant `kynebbrr` of the KY package. We employed this model using the same spectral parameters from the fit of the `kerrbb` model with only free parameters to be the optical depth τ and χ_0. The spin was set to $a = 0.2$ because letting it free will lead to a tight degeneracy with τ. The accretion rate was fixed to $\dot{M} = 0.45 M_{\rm Edd}$, the albedo to 0, and the normalization to 1. We obtained a very good fit with $\chi^2/\nu = 15/20 \approx 0.75$. The $\chi^2/\nu < 1$ indicates that the errors might be overestimated. The best-fit parameters are $\chi_0 = 45° \pm 6°$ and $\tau = 5^{+4}_{-3}$. The PD and PA using this model are shown in Figure 2 (green dotted–dashed line), showing the increasing trend of the PD with energy and being more consistent with the measurements at high energies.

The trend of increasing PD with energy and roughly constant PA seems, nevertheless, to be typical for observations of BHXRBs in the high/soft state. A comparison of the behavior of the PD with energy for three BHXRBs in the high/soft state is shown in Figure 7, where a similar trend is apparent for all sources. Various explanations have been proposed, and different scenarios might be responsible for the observed trend in different sources. In the most prominent case of 4U 1630-47, the PD increase with energy is statistically very significant. A possible explanation attributes this to absorption in the upper

layer of the accretion disk in combination with a relativistic bulk motion, which could also explain a higher PD than expected from an accretion disk with an electron-scattering-dominated atmosphere (Ratheesh et al. 2023). For 4U 1957 +11, the increase can be explained by a combination of a high spin value and high albedo (Marra et al., in preparation). High albedo is, however, unlikely in the case of LMC X-3 given the low value of the black hole spin. To perform a robust statistical test of the significance of the PD's increase with energy, a longer observation would be needed to obtain a significant measurement up to 8 keV.

5. Conclusions

We report on the first X-ray polarimetric observation of the accreting stellar-mass black hole LMC X-3 with the IXPE. The polarization is significantly detected with the PD being $3.2\% \pm 0.6\%$ and PA measured as $-42^\circ \pm 6^\circ$ in the 2–8 keV energy band. We performed a spectropolarimetric fit, including the accompanying observations by the NICER, NuSTAR, and Swift satellites, showing that the X-ray spectrum is best modeled by a slim accretion disk with an intrinsic luminosity of $L \approx 0.4\, L_{\rm Edd}$. We used the spectral data to measure the black hole spin $a \approx 0.2$. Using solely the polarimetric normalized Stokes parameters Q/I and U/I, we obtained for the black hole spin $a < 0.7$ at a 90% confidence level, in agreement with the spectroscopic measurements.

Acknowledgments

The Imaging X-ray Polarimetry Explorer (IXPE) is a joint US and Italian mission. The US contribution is supported by the National Aeronautics and Space Administration (NASA) and led and managed by its Marshall Space Flight Center (MSFC), with industry partner Ball Aerospace (contract NNM15AA18C). The Italian contribution is supported by the Italian Space Agency (Agenzia Spaziale Italiana, ASI) through contract ASI-OHBI-2022-13-I.0, agreements ASI-INAF-2022-19-HH.0 and ASI-INFN-2017.13-H0, and its Space Science Data Center (SSDC) with agreements ASI-INAF-2022-14-HH.0 and ASI-INFN 2021-43-HH.0, and by the Istituto Nazionale di Astrofisica (INAF) and the Istituto Nazionale di Fisica Nucleare (INFN) in Italy. This research used data products provided by the IXPE Team (MSFC, SSDC, INAF, and INFN) and distributed with additional software tools by the High-Energy Astrophysics Science Archive Research Center (HEASARC), at NASA Goddard Space Flight Center (GSFC). This work made use of data supplied by the UK Swift Science Data Centre at the University of Leicester.

The authors thank the referee for insightful comments and suggestions. J.S., M.D., J.P., M.B., and V.K. thank GACR project 21-06825X for the support and institutional support from RVO:67985815. A.Y. and M.B. acknowledge the support from GAUK project No. 102323. A.I. acknowledges support from the Royal Society. A.V. thanks the Academy of Finland grant 355672 for support. P.-O.P. acknowledges financial support from the French Space Agency (CNES) and the French High Energy National Programme (PNHE) of CNRS. N.R.C., M.R. M., H.K., K.H., and S.C. acknowledge support by NASA grants 80NSSC22K1291, 80NSSC23K1041, and 80NSSC20K0329.

Facilities: IXPE, NICER, NuSTAR, Swift.

ORCID iDs

Jiří Svoboda https://orcid.org/0000-0003-2931-0742
Michal Dovčiak https://orcid.org/0000-0003-0079-1239
James F. Steiner https://orcid.org/0000-0002-5872-6061
Fabio Muleri https://orcid.org/0000-0003-3331-3794
Adam Ingram https://orcid.org/0000-0002-5311-9078
Anastasiya Yilmaz https://orcid.org/0000-0003-1133-1684
Nicole Rodriguez Cavero https://orcid.org/0000-0001-5256-0278
Lorenzo Marra https://orcid.org/0009-0001-4644-194X
Juri Poutanen https://orcid.org/0000-0002-0983-0049
Alexandra Veledina https://orcid.org/0000-0002-5767-7253
Mehrnoosh Rahbardar Mojaver https://orcid.org/0000-0002-9633-0359
Stefano Bianchi https://orcid.org/0000-0002-4622-4240
Javier A. García https://orcid.org/0000-0003-3828-2448
Philip Kaaret https://orcid.org/0000-0002-3638-0637
Henric Krawczynski https://orcid.org/0000-0002-1084-6507
Giorgio Matt https://orcid.org/0000-0002-2152-0916
Jakub Podgorný https://orcid.org/0000-0001-5418-291X
Martin C. Weisskopf https://orcid.org/0000-0002-5270-4240
Fabian Kislat https://orcid.org/0000-0001-7477-0380
Pierre-Olivier Petrucci https://orcid.org/0000-0001-6061-3480
Maimouna Brigitte https://orcid.org/0009-0004-1197-5935
Michal Bursa https://orcid.org/0000-0003-0167-1888
Sergio Fabiani https://orcid.org/0000-0003-1533-0283
Kun Hu https://orcid.org/0000-0002-9705-7948
Sohee Chun https://orcid.org/0009-0002-2488-5272
Guglielmo Mastroserio https://orcid.org/0000-0003-4216-7936
Romana Mikušincová https://orcid.org/0000-0001-7374-843X
Ajay Ratheesh https://orcid.org/0000-0003-0411-4243
Roger W. Romani https://orcid.org/0000-0001-6711-3286
Paolo Soffitta https://orcid.org/0000-0002-7781-4104
Francesco Ursini https://orcid.org/0000-0001-9442-7897
Silvia Zane https://orcid.org/0000-0001-5326-880X
Iván Agudo https://orcid.org/0000-0002-3777-6182
Lucio A. Antonelli https://orcid.org/0000-0002-5037-9034
Matteo Bachetti https://orcid.org/0000-0002-4576-9337
Luca Baldini https://orcid.org/0000-0002-9785-7726
Wayne H. Baumgartner https://orcid.org/0000-0002-5106-0463
Ronaldo Bellazzini https://orcid.org/0000-0002-2469-7063
Stephen D. Bongiorno https://orcid.org/0000-0002-0901-2097
Raffaella Bonino https://orcid.org/0000-0002-4264-1215
Alessandro Brez https://orcid.org/0000-0002-9460-1821
Niccolò Bucciantini https://orcid.org/0000-0002-8848-1392
Fiamma Capitanio https://orcid.org/0000-0002-6384-3027
Simone Castellano https://orcid.org/0000-0003-1111-4292
Elisabetta Cavazzuti https://orcid.org/0000-0001-7150-9638
Chien-Ting Chen https://orcid.org/0000-0002-4945-5079
Stefano Ciprini https://orcid.org/0000-0002-0712-2479
Enrico Costa https://orcid.org/0000-0003-4925-8523
Alessandra De Rosa https://orcid.org/0000-0001-5668-6863
Ettore Del Monte https://orcid.org/0000-0002-3013-6334

Laura Di Gesu https://orcid.org/0000-0002-5614-5028
Niccolò Di Lalla https://orcid.org/0000-0002-7574-1298
Alessandro Di Marco https://orcid.org/0000-0003-0331-3259
Immacolata Donnarumma https://orcid.org/0000-0002-4700-4549
Victor Doroshenko https://orcid.org/0000-0001-8162-1105
Steven R. Ehlert https://orcid.org/0000-0003-4420-2838
Teruaki Enoto https://orcid.org/0000-0003-1244-3100
Yuri Evangelista https://orcid.org/0000-0001-6096-6710
Riccardo Ferrazzoli https://orcid.org/0000-0003-1074-8605
Shuichi Gunji https://orcid.org/0000-0002-5881-2445
Jeremy Heyl https://orcid.org/0000-0001-9739-367X
Wataru Iwakiri https://orcid.org/0000-0002-0207-9010
Svetlana G. Jorstad https://orcid.org/0000-0001-6158-1708
Vladimír Karas https://orcid.org/0000-0002-5760-0459
Jeffery J. Kolodziejczak https://orcid.org/0000-0002-0110-6136
Fabio La Monaca https://orcid.org/0000-0001-8916-4156
Luca Latronico https://orcid.org/0000-0002-0984-1856
Ioannis Liodakis https://orcid.org/0000-0001-9200-4006
Simone Maldera https://orcid.org/0000-0002-0698-4421
Alberto Manfreda https://orcid.org/0000-0002-0998-4953
Frédéric Marin https://orcid.org/0000-0003-4952-0835
Andrea Marinucci https://orcid.org/0000-0002-2055-4946
Alan P. Marscher https://orcid.org/0000-0001-7396-3332
Herman L. Marshall https://orcid.org/0000-0002-6492-1293
Francesco Massaro https://orcid.org/0000-0002-1704-9850
Tsunefumi Mizuno https://orcid.org/0000-0001-7263-0296
Michela Negro https://orcid.org/0000-0002-6548-5622
Chi-Yung Ng https://orcid.org/0000-0002-5847-2612
Stephen L. O'Dell https://orcid.org/0000-0002-1868-8056
Nicola Omodei https://orcid.org/0000-0002-5448-7577
Chiara Oppedisano https://orcid.org/0000-0001-6194-4601
Alessandro Papitto https://orcid.org/0000-0001-6289-7413
George G. Pavlov https://orcid.org/0000-0002-7481-5259
Abel L. Peirson https://orcid.org/0000-0001-6292-1911
Matteo Perri https://orcid.org/0000-0003-3613-4409
Melissa Pesce-Rollins https://orcid.org/0000-0003-1790-8018
Maura Pilia https://orcid.org/0000-0001-7397-8091
Andrea Possenti https://orcid.org/0000-0001-5902-3731
Simonetta Puccetti https://orcid.org/0000-0002-2734-7835
Brian D. Ramsey https://orcid.org/0000-0003-1548-1524
John Rankin https://orcid.org/0000-0002-9774-0560
Oliver J. Roberts https://orcid.org/0000-0002-7150-9061
Carmelo Sgrò https://orcid.org/0000-0001-5676-6214
Patrick Slane https://orcid.org/0000-0002-6986-6756
Gloria Spandre https://orcid.org/0000-0003-0802-3453
Douglas A. Swartz https://orcid.org/0000-0002-2954-4461
Toru Tamagawa https://orcid.org/0000-0002-8801-6263
Fabrizio Tavecchio https://orcid.org/0000-0003-0256-0995
Roberto Taverna https://orcid.org/0000-0002-1768-618X
Allyn F. Tennant https://orcid.org/0000-0002-9443-6774
Nicholas E. Thomas https://orcid.org/0000-0003-0411-4606
Francesco Tombesi https://orcid.org/0000-0002-6562-8654
Alessio Trois https://orcid.org/0000-0002-3180-6002
Sergey S. Tsygankov https://orcid.org/0000-0002-9679-0793
Roberto Turolla https://orcid.org/0000-0003-3977-8760
Jacco Vink https://orcid.org/0000-0002-4708-4219
Kinwah Wu https://orcid.org/0000-0002-7568-8765
Fei Xie https://orcid.org/0000-0002-0105-5826

References

Arnaud, K. A. 1996, in ASP Conf. Ser. 101, Astronomical Data Analysis Software and Systems V, ed. G. H. Jacoby & J. Barnes (San Francisco, CA: ASP), 17
Baldini, L., Bucciantini, N., Lalla, N. D., et al. 2022, SoftX, 19, 101194
Belloni, T. M. 2010, in The Jet Paradigm, ed. T. Belloni, Vol. 794 (Berlin: Springer), 53
Bhuvana, G. R., Radhika, D., & Nandi, A. 2022, AdSpR, 69, 483
Blackburn, J. K. 1995, in ASP Conf. Ser. 77, Astronomical Data Analysis Software and Systems IV, ed. R. A. Shaw, H. E. Payne, & J. J. E. Hayes (San Francisco, CA: ASP), 367
Burrows, D. N., Hill, J. E., Nousek, J. A., et al. 2005, SSRv, 120, 165
Chandrasekhar, S. 1960, Radiative Transfer (New York: Dover)
Connors, P. A., Piran, T., & Stark, R. F. 1980, ApJ, 235, 224
Connors, P. A., & Stark, R. F. 1977, Natur, 269, 128
Cunningham, C. 1976, ApJ, 208, 534
Done, C., Gierliński, M., & Kubota, A. 2007, A&ARv, 15, 1
Dovciak, M., Steiner, J. F., Krawczynski, H., & Svoboda, J. 2023, ATel, 16084, 1
Dovčiak, M., Karas, V., & Yaqoob, T. 2004, ApJS, 153, 205
Dovčiak, M., Muleri, F., Goosmann, R. W., Karas, V., & Matt, G. 2008, MNRAS, 391, 32
Ebisawa, K., Makino, F., Mitsuda, K., et al. 1993, ApJ, 403, 684
Evans, P. A., Beardmore, A. P., Page, K. L., et al. 2009, MNRAS, 397, 1177
Fender, R. P., Southwell, K., & Tzioumis, A. K. 1998, MNRAS, 298, 692
Frank, J., King, A., & Raine, D. J. 2002, Accretion Power in Astrophysics (3rd ed.; Cambridge: Cambridge Univ. Press), 398
Gallo, E., Fender, R. P., & Pooley, G. G. 2003, MNRAS, 344, 60
Gehrels, N., Chincarini, G., Giommi, P., et al. 2004, ApJ, 611, 1005
Gendreau, K. C., Arzoumanian, Z., & Okajima, T. 2012, Proc. SPIE, 8443, 844313
Gierliński, M., & Done, C. 2004, MNRAS, 347, 885
Hakala, P. J., Muhli, P., & Dubus, G. 1999, MNRAS, 306, 701
Harrison, F. A., Craig, W. W., Christensen, F. E., et al. 2013, ApJ, 770, 103
HI4PI Collaboration, Ben Bekhti, N., Flöer, l., et al. 2016, A&A, 594, A116
Hubeny, I., & Lanz, T. 1995, ApJ, 439, 875
Hutchings, J. B., Winter, K., Cowley, A. P., Schmidtke, P. C., & Crampton, D. 2003, AJ, 126, 2368
Kaastra, J. S., & Bleeker, J. A. M. 2016, A&A, 587, A151
Krawczynski, H., Muleri, F., Dovčiak, M., et al. 2022, Sci, 378, 650
Lang, C. C., Kaaret, P., Corbel, S., & Mercer, A. 2007, ApJ, 666, 79
Leong, C., Kellogg, E., Gursky, H., Tananbaum, H., & Giacconi, R. 1971, ApJL, 170, L67
Li, L.-X., Zimmerman, E. R., Narayan, R., & McClintock, J. E. 2005, ApJS, 157, 335
Marra, L., Brigitte, M., Rodriguez Cavero, N., et al. 2023, arXiv:2310.11125
McClintock, J. E., Narayan, R., & Steiner, J. F. 2014, SSRv, 183, 295
Mikusincova, R., Dovciak, M., Bursa, M., et al. 2023, MNRAS, 519, 6138
Mitsuda, K., Inoue, H., Koyama, K., et al. 1984, PASJ, 36, 741
Novikov, I. D., & Thorne, K. S. 1973, Black Holes (Les Astres Occlus) (New York: Gordon & Breach), 343
Nowak, M. A., Wilms, J., Heindl, W. A., et al. 2001, MNRAS, 320, 316
Orosz, J. A., Steeghs, D., McClintock, J. E., et al. 2009, ApJ, 697, 573
Orosz, J. A., Steiner, J. F., McClintock, J. E., et al. 2014, ApJ, 794, 154
Page, M. J., Soria, R., Wu, K., et al. 2003, MNRAS, 345, 639
Pietrzyński, G., Graczyk, D., Gallenne, A., et al. 2019, Natur, 567, 200
Podgorny, J., Marra, L., Muleri, F., et al. 2023, MNRAS, 526, 5964
Poutanen, J., Veledina, A., & Beloborodov, A. M. 2023, ApJL, 949, L10
Ratheesh, A., Dovčiak, M., Krawczynski, H., et al. 2023, arXiv:2304.12752
Rees, M. J. 1975, MNRAS, 171, 457
Remillard, R. A., Loewenstein, M., Steiner, J. F., et al. 2022, AJ, 163, 130
Rodriguez Cavero, N., Marra, L., Krawczynski, H., et al. 2023, ApJL, 958, L8
Schnittman, J. D., & Krolik, J. H. 2009, ApJ, 701, 1175
Shafee, R., McClintock, J. E., Narayan, R., et al. 2006, ApJL, 636, L113
Shakura, N. I., & Sunyaev, R. A. 1973, A&A, 500, 33
Sądowski, A., Abramowicz, M., Bursa, M., et al. 2011, A&A, 527, A17
Smale, A. P., & Boyd, P. T. 2012, ApJ, 756, 146
Sobolev, V. V. 1963, A Treatise on Radiative Transfer (Princeton, NJ: Van Nostrand-Reinhold)

Soffitta, P., Baldini, L., Bellazzini, R., et al. 2021, AJ, 162, 208
Steiner, J. F., McClintock, J. E., Orosz, J. A., et al. 2014, ApJL, 793, L29
Steiner, J. F., McClintock, J. E., Remillard, R. A., et al. 2010, ApJL, 718, L117
Steiner, J. F., Narayan, R., McClintock, J. E., & Ebisawa, K. 2009, PASP, 121, 1279
Straub, O., Bursa, M., Sądowski, A., et al. 2011, A&A, 533, A67
Sunyaev, R. A., & Titarchuk, L. G. 1980, A&A, 86, 121
Taverna, R., Zhang, W., Dovčiak, M., et al. 2020, MNRAS, 493, 4960
Torpin, T. J., Boyd, P. T., Smale, A. P., & Valencic, L. A. 2017, ApJ, 849, 32
Treves, A., Belloni, T., Chiappetti, L., et al. 1988, ApJ, 325, 119
Veledina, A., Muleri, F., Poutanen, J., et al. 2023, arXiv:2303.01174
Wang, J., Mastroserio, G., Kara, E., et al. 2021, ApJL, 910, L3
Weisskopf, M. C., Elsner, R. F., & O'Dell, S. L. 2010, Proc. SPIE, 7732, 77320E
Weisskopf, M. C., Soffitta, P., Baldini, L., et al. 2022, JATIS, 8, 026002
Wilms, J., Allen, A., & McCray, R. 2000, ApJ, 542, 914
Wilms, J., Nowak, M. A., Pottschmidt, K., et al. 2001, MNRAS, 320, 327
Wu, K., Soria, R., Page, M. J., et al. 2001, A&A, 365, L267
Yilmaz, A., Svoboda, J., Grinberg, V., et al. 2023, MNRAS, 525, 1288
Zdziarski, A. A., & Gierliński, M. 2004, PThPS, 155, 99